

# Polar stratospheric nitric acid depletion surveyed from a decadal dataset of IASI total columns

Catherine Wespes<sup>1,a,\*</sup>, Gaetane Ronsmans<sup>1,a</sup>, Lieven Clarisse<sup>1</sup>, Susan Solomon<sup>2</sup>, Daniel Hurtmans<sup>1</sup>, Cathy Clerbaux<sup>1,3</sup>, and Pierre-François Coheur<sup>1</sup>

<sup>1</sup>Université libre de Bruxelles (ULB), Spectroscopy, Quantum Chemistry and Atmospheric Remote Sensing (SQUARES), Brussels, Belgium

<sup>2</sup>Department of Earth, Atmospheric and Planetary Sciences, Massachusetts Institute of Technology, Cambridge, Massachusetts, USA

<sup>3</sup>LATMOS/IPSL, Sorbonne Université, UVSQ, CNRS, Paris, France

<sup>a</sup> Co-first authors

\* Corresponding author: Catherine Wespes (catherine.wespes@ulb.be)

## Abstract

In this paper, we exploit the first 10-year data-record (2008-2017) of nitric acid (HNO<sub>3</sub>) total columns measured by the IASI-A/Metop infrared sounder, characterized by an exceptional daily sampling and a good vertical sensitivity in the lower-to-mid stratosphere (around 50 hPa), to monitor the relationship between the temperature decrease and the observed HNO<sub>3</sub> loss that occurs each year in the Antarctic stratosphere during the polar night. Since the HNO<sub>3</sub> depletion results from the formation of polar stratospheric clouds (PSCs) which trigger the development of the ozone (O<sub>3</sub>) hole, its continuous monitoring is of high importance. We verify here, from the 10-year time evolution of HNO<sub>3</sub> together with temperature (taken from reanalysis at 50 hPa), the recurrence of specific regimes in the annual cycle of IASI HNO<sub>3</sub> and identify, for each year, the day and the 50 hPa temperature ("drop temperature") corresponding to the onset of strong HNO<sub>3</sub> depletion in the Antarctic winter. Although the measured HNO<sub>3</sub> total column does not allow the uptake of HNO<sub>3</sub> by different types of PSC particles along the vertical profile to be differentiated, an average drop temperature of  $194.2 \pm 3.8$  K, close to the nitric acid trihydrate (NAT) existence threshold ( $\sim 195$  K at 50 hPa), is found in the region of potential vorticity lower than  $-10 \times 10^{-5}$  K.m<sup>2</sup>.kg<sup>-1</sup>.s<sup>-1</sup> (similar to the 70° – 90° S equivalent latitude region during winter). The spatial distribution and inter-annual variability of the drop temperature are investigated and discussed. This paper highlights the capability of the IASI sounder to monitor the evolution of polar stratospheric HNO<sub>3</sub>, a key player in the processes involved in the depletion of stratospheric O<sub>3</sub>.

## 1 Introduction

The cold and isolated air masses found within the polar vortex during winter are associated with a strong denitrification of the stratosphere due to the formation of PSCs (composed of HNO<sub>3</sub>, sulphuric acid (H<sub>2</sub>SO<sub>4</sub>) and water ice (H<sub>2</sub>O)) (e.g. Peter, 1997; Voigt et al., 2000; von König, 2002; Schreiner et al., 2003; Peter and Groö, 2012). These clouds strongly affect the polar chemistry by (1) acting as surfaces for the heterogeneous activation of chlorine and bromine compounds, in turn leading to enhanced O<sub>3</sub> destruction (e.g. Solomon, 1999; Wang and Michelangeli, 2006; Harris et al., 2010; Wegner et al., 2012) and by (2) removing gas-phase HNO<sub>3</sub> temporarily or permanently through uptake by PSCs and sedimentation of large PSC particles to lower altitudes. The denitrification of the polar stratosphere during winter delays the reformation of ClONO<sub>2</sub>, a chlorine reservoir, and, hence, intensifies the O<sub>3</sub> hole (e.g. Solomon, 1999; Harris et al., 2010; Tritscher et al., 2021). The heterogeneous reaction rates on PSC surfaces and the uptake of HNO<sub>3</sub> strongly depend on the temperature and on the PSC particle type. The

49 PSCs are classified into three different types based on their composition and optical properties: type Ia  
50 solid nitric acid trihydrate - NAT ( $\text{HNO}_3 \cdot (\text{H}_2\text{O})_3$ ), type Ib liquid supercooled ternary solution - STS  
51 ( $\text{HNO}_3/\text{H}_2\text{SO}_4/\text{H}_2\text{O}$  with variable composition) and type II, crystalline water-ice particles (likely  
52 composed of a combination of different chemical phases) (e.g. Toon et al., 1986; Koop et al., 2000;  
53 Voigt et al., 2000; Lowe and MacKenzie, 2008). In the stratosphere, they mostly consist of mixtures of  
54 liquid/solid STS/NAT particles in varying number densities, with  $\text{HNO}_3$  being the major constituent of  
55 these particles. The large-size NAT particles of low number density are the principal cause of  
56 sedimentation (Lambert et al., 2012; Pitts et al., 2013; Molleker et al., 2014; Lambert et al., 2016). The  
57 formation temperature of STS ( $T_{STS}$ ) and the thermodynamic equilibrium temperatures of NAT ( $T_{NAT}$ )  
58 and ice ( $T_{ice}$ ) have been determined, respectively, as:  $\sim 192$  K (Carslaw et al., 1995),  $\sim 195.7$  K (Hanson  
59 and Mauersberger, 1988) and  $\sim 188$  K (Murphy and Koop, 2005) for typical 50 hPa atmospheric  
60 conditions (5 ppmv  $\text{H}_2\text{O}$  and 10 ppbv  $\text{HNO}_3$ ). While the NAT nucleation was thought to require pre-  
61 existing ice nuclei, hence, temperatures below  $T_{ice}$  (e.g. Zondlo et al., 2000; Voigt et al., 2003), recent  
62 observational and modelling studies have shown that  $\text{HNO}_3$  starts to condense in early PSC season in  
63 liquid NAT mixtures well above  $T_{ice}$  ( $\sim 4$  K below  $T_{NAT}$ , close to  $T_{STS}$ ) even after a very short temperature  
64 threshold exposure (TTE) to these temperatures but also slightly below  $T_{NAT}$  after a long TTE, whereas  
65 the NAT existence persists up to  $T_{NAT}$  (Pitts et al., 2013; Hoyle et al., 2013; Lambert et al., 2016; Pitts  
66 et al., 2018). It has been recently proposed that the higher temperature condensation results from  
67 heterogeneous nucleation of NAT on meteoritic dust in liquid aerosol (Voigt et al., 2005; Hoyle et al.,  
68 2013; Grooß et al., 2014; James et al., 2018; Tritscher et al., 2021). Further cooling below  $T_{STS}$  and  $T_{ice}$   
69 leads to nucleation of liquid STS, of solid NAT onto ice and of ice particles mainly from STS (type II  
70 PSCs) (Lowe and MacKenzie, 2008). The formation of NAT and ice has also been shown to be triggered  
71 by stratospheric mountain-waves (Carslaw et al., 1998; Hoffmann et al., 2017). Although the formation  
72 mechanisms and composition of STS droplets in stratospheric conditions are well described (Toon et al.,  
73 1986; Carslaw et al., 1995; Lowe and MacKenzie, 2008), the NAT and ice nucleation processes still  
74 require further investigation (Tritscher et al., 2021). This could be important as the chemistry-climate  
75 models (CCMs) generally oversimplify the heterogeneous nucleation schemes for PSC formation (Zhu  
76 et al., 2015; Spang et al., 2018; Snels et al., 2019), preventing an accurate estimation of  $\text{O}_3$  levels.

77  
78 Over the last few decades, several satellite instruments have measured stratospheric  $\text{HNO}_3$  (e.g.  
79 MLS/UARS (Santee et al., 1999), MLS/Aura (Santee et al., 2007), MIPAS/ENVISAT (Piccolo and  
80 Dudhia, 2007), ACE-FTS/SCISAT (Sheese et al., 2017) and SMR/Odin (Urban et al., 2009)).  
81 Spaceborne instruments such as the CALIOP/CALIPSO lidar and MIPAS/Envisat measuring in the  
82 infrared are capable of detecting and classifying PSC types, allowing their formation mechanisms to be  
83 investigated (Lambert et al., 2016; Pitts et al., 2018; Spang et al., 2018, Tritscher et al., 2021 and  
84 references therein); these satellite data complement in situ measurements (Voigt et al., 2005) and ground-  
85 based lidar (Snels et al., 2019). From these available observational datasets,  $\text{HNO}_3$  depletion has been  
86 linked to PSC formation and detected below the  $T_{NAT}$  threshold (Santee et al., 1999; Urban et al., 2009;  
87 Lambert et al., 2016; Ronsmans et al., 2018), but its relationship to PSCs still needs further investigation  
88 given the complexity of the nucleation mechanisms that depend on several parameters (e.g. atmospheric  
89 temperature, water and  $\text{HNO}_3$  vapour pressure, time exposure to temperatures, temperature history).

90  
91 In contrast to the limb satellite instruments mentioned above, the infrared nadir sounder IASI offers a  
92 dense spatial sampling of the entire globe, twice a day (Section 2). While it cannot provide a vertical  
93 profile of  $\text{HNO}_3$  similar to that from the limb sounders, IASI provides reliable total column  
94 measurements of  $\text{HNO}_3$  characterized by a maximum sensitivity in the low-middle stratosphere around  
95 50 hPa (20 km) during the dark Antarctic winter (Ronsmans et al., 2016, 2018) where PSCs form (Voigt  
96 et al., 2005; Lambert et al., 2012; Spang et al., 2016, 2018). This study aims to explore the 10-year  
97 continuous  $\text{HNO}_3$  measurements from IASI to provide a long-term global picture of depletion and of its

98 dependence on temperatures during polar winter (Section 3). The temperature corresponding to the onset  
99 of the strong depletion in HNO<sub>3</sub> records (here referred to as ‘drop temperature’) is identified in Section  
100 4 for each observed year and discussed in the context of previous studies.

101

## 102 **2 Data**

103

104 The HNO<sub>3</sub> data used in the present study are obtained from measurements of the Infrared Atmospheric  
105 Sounding Interferometer (IASI) onboard the Metop-A satellite. IASI measures the Earth’s and  
106 atmosphere’s radiation in the thermal infrared spectral range (645 - 2760 cm<sup>-1</sup>), with a 0.5 cm<sup>-1</sup> apodized  
107 resolution and a low radiometric noise (Clerbaux et al., 2009; Hilton et al., 2012). Thanks to its polar  
108 sun-synchronous orbit with more than 14 orbits a day and a field of view of four simultaneous footprints  
109 of 12 km at nadir, IASI provides global coverage twice a day (9.30 AM and PM mean local solar time).  
110 That extensive spatial and temporal sampling in the polar regions is key to this study.

111

112 The HNO<sub>3</sub> vertical profiles are retrieved on a uniform vertical 1 km grid of 41 layers (from the surface  
113 to 40 km with an extra layer above to 60 km) in near-real-time by the Fast Optimal Retrieval on Layers  
114 for IASI (FORLI) software, using the optimal estimation method (Rodgers, 2000). Detailed information  
115 on the FORLI algorithm and retrieval parameters specific to HNO<sub>3</sub> can be found in previous papers  
116 (Hurtmans et al., 2012; Ronsmans et al., 2016). For this study, only the total columns (v20151001) are  
117 used, considering (1) the low vertical resolution of IASI with only one independent piece of information  
118 (full width at half maximum - FWHM - of the averaging kernels of ~30 km), (2) the limited sensitivity  
119 of IASI to tropospheric HNO<sub>3</sub>, (3) the dominant contribution of the stratosphere to the HNO<sub>3</sub> total  
120 column and (4) the largest sensitivity of IASI in the region of interest, i.e. in the low and mid-stratosphere  
121 (from ~70 to ~30 hPa), where the HNO<sub>3</sub> abundance is the highest (Ronsmans et al., 2016). The IASI  
122 measurements capture the expected depletion of HNO<sub>3</sub> within the polar night, as illustrated in Fig. 1 that  
123 shows examples of vertical HNO<sub>3</sub> profiles retrieved within the dark Antarctic vortex (above Arrival  
124 Heights) and outside the vortex (above Lauder). The retrieved profiles are shown along with their  
125 associated total retrieval error and averaging kernels (the total column averaging kernel and the so-called  
126 “sensitivity profile” are also represented; see Ronsmans et al., 2016 for more details). The total column  
127 averaging kernel (in black) indicates the sensitivity of the total column measurement to changes in the  
128 vertical distribution of HNO<sub>3</sub>, hence, the altitude to which the retrieved total column is mainly  
129 sensitive/representative, while the sensitivity profile indicates the extent to which the retrieval at one  
130 specific altitude comes from the spectral measurement rather than the a priori. Above Arrival Heights  
131 during the dark Antarctic winter, we clearly see depleted HNO<sub>3</sub> levels in the low and mid-stratosphere  
132 and the altitude of maximum sensitivity at around 30 hPa for this case (values of ~1 along the total  
133 column averaging kernel around that level). In contrast, at Lauder, HNO<sub>3</sub> levels larger than the a priori  
134 are observed in the stratosphere with a larger range of maximum sensitivity. The total columns are  
135 associated with a total retrieval error ranging from around 3% at mid- and polar latitudes (except above  
136 Antarctica) to 25% above cold Antarctic surface during winter and with a low absolute bias smaller than  
137 12% when compared to ground-based FTIR measurements, in polar regions over the altitude range  
138 where the IASI sensitivity is the largest (see Hurtmans et al., 2012 and Ronsmans et al., 2016 for more  
139 details). The highest retrieval error measured over the Antarctic arises from a weaker sensitivity above  
140 very cold surface with a degrees of freedom for signal (DOFS) of 0.95, as well as from a poor knowledge  
141 of the seasonally and wavenumber-dependent emissivity above ice surfaces. In order to expand on the  
142 comparisons against FTIR measurements, which cannot be made during the polar night, Fig. 2 (top  
143 panel) presents the time series of daily IASI total HNO<sub>3</sub> columns co-located with MLS measurements  
144 within 2.5°x2.5° grid boxes, averaged in the 70°S–90°S equivalent latitude band. In order to account for  
145 the vertical sensitivity of IASI, the averaging kernels associated with each co-located IASI retrieved  
146 profile were applied to the MLS profiles for this cross-comparison. The MLS mixing ratio profiles over

147 the 215-1.5 hPa pressure range were first interpolated to the FORLI pressure grids and extended down  
148 to the surface by using the FORLI-HNO<sub>3</sub> a priori profile, and then converted into partial columns.  
149 Similar variations in the HNO<sub>3</sub> column are captured by the two instruments, with an excellent agreement  
150 in particular for the timing of the strong HNO<sub>3</sub> depletion within the inner vortex core. Note that a similar  
151 good agreement between the two satellite datasets is obtained in other latitude bands (see Fig. 2 bottom  
152 panel for the 50°S–70°S equivalent latitude band; the other bands are not shown).

153  
154 Quality flags similar to those developed for O<sub>3</sub> in previous IASI studies (Wespes et al., 2017) were  
155 applied a posteriori to exclude data (i) with a corresponding poor spectral fit (e.g. based on quality flags  
156 rejecting biased or sloped residuals, fits with maximum number of iterations exceeded), (ii) with less  
157 reliability (e.g. based on quality flags rejecting suspect averaging kernels, data with less sensitivity  
158 characterized by a DOFS lower than 0.9) or (iii) with tropospheric cloud contamination (defined by a  
159 fractional cloud cover  $\geq 25\%$ ). Note that the HNO<sub>3</sub> total column distributions illustrated in sections  
160 below use the median as a statistical average since it is more robust against the outliers than the mean.

161  
162 Temperature and potential vorticity (PV) fields are taken from the ECMWF ERA Interim Reanalysis  
163 dataset, respectively at 50 hPa and at the potential temperature of 530 K (corresponding to  $\sim 20$  km  
164 altitude where the IASI sensitivity to HNO<sub>3</sub> is the highest during the Southern Hemisphere (S.H.) winter  
165 (Ronsmans et al., 2016)). Because the HNO<sub>3</sub> uptake by PSCs starts within a few degrees below  $T_{NAT}$   
166 ( $\sim 195.7$  K at 50 hPa (Hanson and Mauersberger, 1988)) depending on the meteorological conditions  
167 (Pitts et al., 2013; Hoyle et al., 2013; Lambert et al., 2016; Pitts et al., 2018), a threshold temperature of  
168 195 K is considered in the sections below to identify regions of potential PSC existence. The potential  
169 vorticity is used to delimit dynamically consistent areas in the polar regions. In what follows, we use  
170 either the equivalent latitudes ("eqlat", calculated from PV fields at 530 K) or the PV values to  
171 characterize the relationship between HNO<sub>3</sub> and temperatures in the cold polar regions. Uncertainties in  
172 ERA-Interim temperatures will also be discussed below.

### 173 174 **3 Annual cycle of HNO<sub>3</sub> vs temperatures**

175  
176 Figure 3a shows the yearly HNO<sub>3</sub> cycle (solid lines, left axis) in the southernmost equivalent latitudes  
177 (70° - 90° S) as measured by IASI over the whole study period (2008–2017). The total HNO<sub>3</sub> variability  
178 in such equivalent latitudes has already been discussed in a previous IASI study (Ronsmans et al., 2018),  
179 where the contribution of the PSCs to the HNO<sub>3</sub> variations was highlighted. The temperature time series,  
180 taken at 50 hPa, is represented as well (dashed lines, right axis). From this figure, different regimes of  
181 HNO<sub>3</sub> total columns vs temperature can be observed throughout the year and from one year to another.  
182 In particular, we define here three main regimes (R1, R2 and R3) during the HNO<sub>3</sub>/temperature annual  
183 cycle. The full cycle and the main regimes in the 70° - 90° S eqlat region are further represented in Fig.  
184 3b that shows a histogram of the HNO<sub>3</sub> total columns as a function of temperature for the year 2011.  
185 Similar histograms are observed for the other years in the 10-year study period (not shown). The orange  
186 horizontal and vertical lines in Fig. 3a and Fig. 3b, respectively, represent the 195 K threshold  
187 temperature used to identify the onset of HNO<sub>3</sub> uptake by PSCs (see Section 2). The three regimes  
188 identified are:

- 189
- 190 - R1 is defined by the maxima in the total HNO<sub>3</sub> abundances covering the months of April and  
191 May ( $\sim 3 \times 10^{16}$  molec.cm<sup>-2</sup>), when the 50 hPa temperature strongly decreases (from  $\sim 220$  to  $\sim 195$   
192 K). These high HNO<sub>3</sub> levels result from low sunlight, preventing photodissociation, along with  
193 the heterogeneous hydrolysis of N<sub>2</sub>O<sub>5</sub> to HNO<sub>3</sub> during autumn before the formation of polar  
194 stratospheric clouds (Keys et al., 1993; Santee et al., 1999; Urban et al., 2009; de Zafra and  
195 Smyshlyaev, 2001). This period also corresponds to the onset of the development of the southern

196 polar vortex, which is characterized by strong diabatic descent with weak latitudinal mixing  
197 across its boundary, isolating polar HNO<sub>3</sub>-rich air from lower-latitude airmasses. The end of the  
198 R1 period marks the start of the strong total HNO<sub>3</sub> decrease that intensifies later in R2.  
199

- 200 - R2, which extends from June to October, follows the onset of the strong decrease in HNO<sub>3</sub> total  
201 columns that starts around mid-May in most years when the temperatures fall below 195 K. After  
202 a steep initial decline in total HNO<sub>3</sub>, R2 is characterized by a plateau of total HNO<sub>3</sub> minima. For  
203 much of this regime, average HNO<sub>3</sub> total columns are below  $2 \times 10^{16}$  molec.cm<sup>-2</sup> and the 50 hPa  
204 temperatures range mostly between 180 and 190 K.  
205
- 206 - R3 starts in October when sunlight returns and the 50 hPa temperatures rise above 195 K. Despite  
207 50 hPa temperatures increasing up to 240 K in summer, the HNO<sub>3</sub> total columns stagnate at the  
208 R2 plateau levels (around  $1.5 \times 10^{16}$  molec.cm<sup>-2</sup>). This regime likely reflects the photolysis of NO<sub>3</sub>  
209 and HNO<sub>3</sub> itself (Ronsmans et al., 2018) as well as the permanent denitrification of the mid-  
210 stratosphere, caused by sedimentation of PSCs. The likely renitrification of the lowermost  
211 stratosphere (e.g. Braun et al., 2019; Lambert et al., 2012), where the HNO<sub>3</sub> concentrations and  
212 the IASI sensitivity to HNO<sub>3</sub> are lower (Ronsmans et al., 2016), cannot be inferred from the IASI  
213 total column measurements. The plateau lasts until approximately February, when HNO<sub>3</sub> total  
214 column slowly starts increasing, reaching the April-May maximum in R1.  
215

216 As illustrated in Fig. 3a, the three regimes are observed each year with, however, some interannual  
217 variations. For instance, the sudden stratospheric warming (SSW) that occurred in 2010 (see the  
218 temperature time series at 20 hPa for the year 2010; green dotted line) yielded higher HNO<sub>3</sub> total columns  
219 (see green solid line in July - September) (de Laat and van Weele, 2011; Klekociuk et al., 2011; WMO,  
220 2014; Ronsmans et al., 2018).  
221

222 Figure 3c shows the evolution of the relationship between the daily averaged HNO<sub>3</sub> (calculated from a  
223 7-day moving average) with the highest occurrence (in bins of  $0.1 \times 10^{16}$  molec.cm<sup>-2</sup> and of 2K) and the  
224 50 hPa temperature, over the 10-year study period. The orange vertical line represents the 195 K  
225 threshold temperature. Figure 3c also highlights the large interannual variability in total HNO<sub>3</sub> in R3,  
226 while the strong depletion in HNO<sub>3</sub> in R2 is consistent every year. Given that PSC formation spans a  
227 large range of altitudes (typically between 10 and 30 km) (Höpfner et al., 2006, 2009; Spang et al., 2018;  
228 Pitts et al., 2018) and that IASI has maximum sensitivity to HNO<sub>3</sub> around 50 hPa (Hurtmans et al., 2012;  
229 Ronsmans et al., 2016), the temperatures at two other pressure levels, namely 70 and 30 hPa (i.e. ~15  
230 and ~25 km), have also been tested to investigate the relationship between HNO<sub>3</sub> and temperature in the  
231 low and mid-stratosphere. The results (not shown here) exhibit a similar HNO<sub>3</sub>-temperature behavior at  
232 the different levels with, as expected, lower and higher temperatures in R2, respectively, at 30 hPa and  
233 at 70 hPa (temperatures down to ~180 K at 30 hPa and down to ~185 K at 70 hPa, as compared to  
234 temperatures down to ~182 K at 50 hPa, are observed), but still below the NAT formation threshold at  
235 these pressure levels ( $T_{NAT} \sim 193$  K at 30 hPa and ~197 K at 70 hPa) (Lambert et al., 2016). Therefore,  
236 the altitude range of maximum IASI sensitivity to HNO<sub>3</sub> (see Section 2) is characterized by temperatures  
237 that are below the NAT formation threshold at these pressure levels, enabling PSC formation and the  
238 denitrification process. Furthermore, the consistency between the 195 K threshold temperature taken at  
239 50 hPa and the onset of the strong total HNO<sub>3</sub> depletion seen in IASI data (see Fig. 3a) is in agreement  
240 with the largest NAT area that starts to develop in June around 20 km (Spang et al., 2018), which justifies  
241 the use of the 195 K temperature at that single representative level in this study.  
242

#### 243 **4 Onset of HNO<sub>3</sub> depletion and drop temperature detection**

244

245 To identify the spatial and temporal variability of the onset of the depletion phase, the daily time  
246 evolution of HNO<sub>3</sub> during the first 10 years of IASI measurements and the temperatures at 50 hPa are  
247 explored. In particular, the second derivative of HNO<sub>3</sub> total column with respect to time is calculated to  
248 detect the strongest rate of decrease seen in the HNO<sub>3</sub> time series and to identify its associated day and  
249 50 hPa temperature.

250

#### 251 4.1 HNO<sub>3</sub> vs temperature time series

252

253 Figure 4 shows the time series of the second derivative of HNO<sub>3</sub> total column (blue) and of the  
254 temperature (red) with respect to time, averaged in the area of potential vorticity smaller than  $-10 \times 10^{-5}$   
255  $\text{K} \cdot \text{m}^2 \cdot \text{kg}^{-1} \cdot \text{s}^{-1}$  at the potential temperature of 530 K to encompass the region inside the inner polar vortex  
256 where the temperatures are the coldest and the largest depletion of total HNO<sub>3</sub> occurs (Ronsmans et al.,  
257 2018). The use of that PV threshold value explains the gaps in the time series during the summer when  
258 the PV does not reach such low levels, while the time series averaged in the 70°- 90° S equlat band (dashed  
259 blue for the second derivative of HNO<sub>3</sub> and grey for the temperature) covers the full year. Note that the  
260 HNO<sub>3</sub> time series has been smoothed with a simple spline data interpolation function to avoid gaps in  
261 order to calculate the second derivative of HNO<sub>3</sub> total column with respect to time as the daily second-  
262 difference in HNO<sub>3</sub> total columns. The horizontal red line shows the 195 K threshold.

263

264 As already illustrated in Fig. 3a and Fig. 3c, the strongest rate of HNO<sub>3</sub> depletion (i.e. the second  
265 derivative minimum) is found closely around the time that temperatures drop below the 195 K threshold  
266 (except for the year 2009 that shows a longest delay), within a few days to a few weeks (4 to 23 days)  
267 after total HNO<sub>3</sub> reaches its maximum, i.e. between the 11th of May (2013) and the 8th of June (2009).  
268 The 50 hPa drop temperatures, i.e. the temperature associated with the strongest rate of HNO<sub>3</sub> depletion  
269 detected from IASI, are between 189.2 K and 198.6 K, with the exception of the year 2014, which shows  
270 a drop temperature of 202.8 K. On average over the 10 years of studied IASI measurements, a 50 hPa  
271 drop temperature of  $194.2 \text{ K} \pm 3.8 \text{ K}$  ( $1\sigma$  standard deviation) is found. Knowing that  $T_{\text{NAT}}$  can be higher  
272 or lower depending on the atmospheric conditions and that NAT starts to nucleate from  $\sim 2-4 \text{ K}$  below  
273  $T_{\text{NAT}}$  (Pitts et al., 2011; Hoyle et al., 2013; Lambert et al., 2016), the results here tend to demonstrate the  
274 consistency between the 50 hPa drop temperature and the PSC existence temperature in that altitude  
275 region. Note that the range observed in the 50 hPa drop temperature could reflect variations in the  
276 preponderance of one type of PSCs over another from one year to the next. The results further justify  
277 the use of the single 50 hPa level for characterizing and investigating the onset of HNO<sub>3</sub> depletion from  
278 IASI. Nevertheless, given the range of maximum IASI sensitivity to HNO<sub>3</sub> around 50 hPa, typically  
279 between 70 and 30 hPa (Ronsmans et al., 2016), the drop temperatures are also calculated at these two  
280 other pressure levels (not shown here) in order to estimate the uncertainty of the calculated drop  
281 temperature defined in this study at 50 hPa. The 30 hPa and 70 hPa drop temperatures range respectively  
282 over 185.7 K – 194.9 K and over 194.8 K – 203.7 K, with an average of  $192.0 \pm 2.9 \text{ K}$  and  $198.0 \pm 3.2$   
283  $\text{K}$  ( $1\sigma$  standard deviation) over the ten years of IASI. The average values at 30 hPa and 70 hPa fall within  
284 the  $1\sigma$  standard deviation associated with the average drop temperature at 50 hPa. It is also worth noting  
285 the agreement between the drop temperatures and the NAT formation threshold at these two pressure  
286 levels ( $T_{\text{NAT}} \sim 193 \text{ K}$  at 30 hPa and  $\sim 197 \text{ K}$  at 70 hPa) (Lambert et al., 2016). Finally, it should be noted  
287 that, because the size, shape or location of the vortex vary slightly over the altitude range to which IASI  
288 is sensitive (from  $\sim 30$  to  $\sim 70$  hPa during the polar night), the use of a single potential temperature surface  
289 for the calculation of drop temperatures could introduce some uncertainties into the results. However,  
290 several tests suggest that these variations of the vortex are overall minor and, hence, have only limited  
291 influence on the identification of the inner polar vortex (delimited by a PV value of  $-10 \times 10^{-5} \text{ K} \cdot \text{m}^2 \cdot \text{kg}^{-1} \cdot \text{s}^{-1}$   
292 at 530 K) and on the determination of the average drop temperature inside that region.

293

294 Figures 5a and b show the climatological zonal distribution of HNO<sub>3</sub> total columns and of the  
295 temperature at 50 hPa, respectively, spanning the 55° S - 90° S geographic latitude band over the first  
296 ten years of IASI, with, superimposed, three isocontour levels of potential vorticity ( $-10$ ,  $-8$  and  $-5 \times 10^{-5}$   
297  $\text{K} \cdot \text{m}^2 \cdot \text{kg}^{-1} \cdot \text{s}^{-1}$  in blue, cyan and black, respectively) and the isocontours for the 195 K temperature (pink)  
298 and for the averaged 194.2 K drop temperature (purple) at 50 hPa. They further illustrate the relationship  
299 between the IASI total HNO<sub>3</sub> columns and the 50 hPa temperatures. The climatological (2008-2017) PV  
300 isocontour of  $-10 \times 10^{-5} \text{K} \cdot \text{m}^2 \cdot \text{kg}^{-1} \cdot \text{s}^{-1}$  is clearly shown to separate well the region of strong depletion in  
301 total HNO<sub>3</sub>, according to the latitude and the time, until October. The red vertical dashed line indicates  
302 the average of the dates on which the 50 hPa drop temperatures are calculated in the area of  $\text{PV} \leq -10 \times 10^{-5}$   
303  $\text{K} \cdot \text{m}^2 \cdot \text{kg}^{-1} \cdot \text{s}^{-1}$  ( $194.2 \pm 3.8 \text{ K}$ ; see Fig. 4) over the first ten years of IASI. It shows that the strongest rate  
304 of HNO<sub>3</sub> depletion occurs on average at the end of May (24 May), a few days after the temperature  
305 decreases below 195 K. The yearly zonally averaged time series over the 10-year study period can be  
306 found in Fig. 6, which shows that IASI measures similar HNO<sub>3</sub> total column zonal distributions every  
307 year, in particular with respect to the edge of the collar region and of the region of strong depletion  
308 (respectively delimited by the PV isocontours of  $-5 \times 10^{-5} \text{K} \cdot \text{m}^2 \cdot \text{kg}^{-1} \cdot \text{s}^{-1}$  and of  $-10 \times 10^{-5} \text{K} \cdot \text{m}^2 \cdot \text{kg}^{-1} \cdot \text{s}^{-1}$  at  
309 530 K). Like for Fig.4, an exact timing or a few days between the time that temperatures drop below the  
310 195 K threshold and the start of the HNO<sub>3</sub> depletion is visible every year in Fig. 6. A longest delay is  
311 also observed for the year 2009. Note that the mismatch between the 10-year average of the dates on  
312 which the 195 K threshold temperature is reached and that of the dates for the drop temperatures (see  
313 Fig. 5 a and b) is driven by the year 2013, which is characterized by the lowest temperatures during the  
314 Antarctic winter over the 10-year study period and, hence, the earliest date for the drop temperature  
315 (11th of May; see Fig. 4 and Fig. 6).

## 316 317 **4.2 Spatial distribution of drop temperatures**

318  
319 To explore the capability of IASI to monitor the onset of HNO<sub>3</sub> depletion at a large scale, figure 7 shows,  
320 for each year of the study period, the spatial distribution of the 50 hPa drop temperatures based on the  
321 second derivative minima of total HNO<sub>3</sub> averaged in  $1^\circ \times 1^\circ$  grid cells. The region of interest here is  
322 delimited by a PV value of  $-8 \times 10^{-5} \text{K} \cdot \text{m}^2 \cdot \text{kg}^{-1} \cdot \text{s}^{-1}$  at 530 K, in order to investigate an area a bit larger  
323 than the inner vortex core that was the focus of the preceding discussion (delineated in green in figure 7  
324 by the PV isocontour of  $-10 \times 10^{-5} \text{K} \cdot \text{m}^2 \cdot \text{kg}^{-1} \cdot \text{s}^{-1}$  averaged over the interval 10 May to 15 July). The  
325 isocontour of  $-10 \times 10^{-5} \text{K} \cdot \text{m}^2 \cdot \text{kg}^{-1} \cdot \text{s}^{-1}$  for the minimum PV (in cyan) encountered at 530 K over the 10  
326 May to 15 July period for each year, as well as the isocontours of 195 K for the average temperatures  
327 and the minimum temperatures, are also represented. The calculated drop temperatures corresponding  
328 to the onset of HNO<sub>3</sub> depletion inside the averaged PV isocontour are found to vary between  $\sim 180$  and  
329  $\sim 210 \text{ K}$  and the corresponding dates range between  $\sim$ mid-May and mid-July (not shown here). Although  
330 the range of drop temperatures and dates for  $1^\circ \times 1^\circ$  bins is broader than that found for the inner vortex  
331 averages discussed above, the results are qualitatively consistent. For example, the year 2014 that shows  
332 the highest inner vortex average drop temperature in Figure 4 is characterized by the highest drop  
333 temperatures above the eastern Antarctic. Note, however, that the high extremes in the drop temperature,  
334 mainly found above the eastern Antarctic, should be considered with caution: they correspond to specific  
335 regions above ice surfaces with emissivity features that are known to yield errors in the IASI retrievals  
336 (Hurtmans et al., 2012; Ronsmans et al., 2016). Indeed, bright land surfaces such as ice might in some  
337 cases lead to poor HNO<sub>3</sub> retrievals. Although wavenumber-dependent surface emissivity atlases are used  
338 in FORLI (Hurtmans et al., 2012), this parameter remains critical and causes poorer retrievals that, in  
339 some instances, pass through the series of quality filters and could affect the drop temperature  
340 calculation.

341

342 The averaged isocontour of 195 K encircles fairly well the area of HNO<sub>3</sub> drop temperatures lower than  
343 195 K (typically from ~187 K to ~195 K), which means that the bins inside that area include airmasses  
344 that experience the NAT threshold temperature during a long time over the 10 May – 15 July period.  
345 That area encompasses the inner vortex core (delimited by the isocontour of  $-10 \times 10^{-5} \text{ K.m}^2.\text{kg}^{-1}.\text{s}^{-1}$  for  
346 the PV averaged over the 10 May – 15 July period) and shows pronounced minima (lower than  $-0.5 \times 10^{14}$   
347 molec.cm<sup>-2</sup>.d<sup>-2</sup>) in the second derivative of the HNO<sub>3</sub> total column with respect to time (not shown here),  
348 which indicate a strong and rapid HNO<sub>3</sub> depletion. The area enclosed between the two isocontours of  
349 195 K for the temperatures, the averaged one and the one for the minimum temperatures, shows generally  
350 higher drop temperatures and weakest minima (larger than  $-0.5 \times 10^{14}$  molec.cm<sup>-2</sup>.d<sup>-2</sup>) in the second  
351 derivative of the HNO<sub>3</sub> total column (not shown). That area is also typically enclosed by the isocontour  
352 of  $-10 \times 10^{-5} \text{ K.m}^2.\text{kg}^{-1}.\text{s}^{-1}$  for the minimum PV, meaning that the bins inside correspond, at least for one  
353 day over the 10 May – 15 July period, to airmasses located at the inner edge of the vortex and  
354 characterized by temperature lower than the NAT threshold temperature. The fact that the weakest  
355 minima in the second derivative of total HNO<sub>3</sub> are observed in that area (not shown) indicates a weak  
356 and slow HNO<sub>3</sub> depletion that might be explained by air masses at the inner edge of the vortex  
357 experiencing only a short period with temperatures below the NAT threshold temperature. It could also  
358 reflect mixing with strongly HNO<sub>3</sub>-depleted and colder airmasses from the inner vortex core. Mixing  
359 with these already depleted airmasses could also explain the higher drop temperatures detected in those  
360 bins. These sometimes unrealistic high drop temperatures are generally detected later (after the strong  
361 HNO<sub>3</sub> depletion occurs in the inner vortex core, i.e. after the 10 May – 15 July period considered here –  
362 not shown), which supports the transport, in those bins, of previously HNO<sub>3</sub>-depleted airmasses and the  
363 likely mixing at the edge of the vortex. Note, however, that previous studies have shown a generally  
364 weak mixing in the Antarctic between the edge region and the vortex core (e.g. Roscoe et al., 2012).  
365 Finally, these spatial variations might also partly reflect some uncertainty in the drop temperature  
366 calculation, introduced by the use of temperature at a single pressure level (50 hPa) and of PV on a single  
367 potential temperature surface (530 K) while the sensitivity of IASI to changes in the HNO<sub>3</sub> profiles  
368 extends over a range from ~30 to ~70 hPa during the polar night. It should be noted that biases in the  
369 ECMWF ERA Interim temperatures used in this work are too small to explain the large range of drop  
370 temperatures calculated here. Indeed, Lambert and Santee (2018) found only a small warm bias, with  
371 median differences around 0.5 K, reaching 0–0.25 K in the southernmost regions of the globe at ~68–21  
372 hPa where PSCs form, through comparisons with the Constellation Observing System for Meteorology,  
373 Ionosphere and Climate (COSMIC) data.

374  
375 Except above some parts of Antarctica which are prone to larger retrieval errors and where unrealistic  
376 high drop temperatures are found, the overall range in the 50 hPa drop temperature for total HNO<sub>3</sub> inside  
377 the isocontour for the averaged temperature of 195 K typically extends from ~187 K to ~195 K, which  
378 falls within the range of PSC nucleation temperature at 50 hPa: from slightly below  $T_{NAT}$  to around 3-4  
379 K below the ice frost point -  $T_{ice}$  - depending on atmospheric conditions, on TTE and on the specific  
380 formation mechanism (i.e., the type of PSC developing) (Pitts et al., 2011; Peter and Grooß, 2012; Hoyle  
381 et al., 2013). This underlines well the benefit of the excellent spatial and temporal coverage of IASI,  
382 which allows the rapid and critical depletion phase to be captured in detail over a large scale.

## 383 384 **5 Conclusions**

385  
386 In this paper, we have explored the added value of the dense HNO<sub>3</sub> total column dataset provided by the  
387 IASI/Metop-A satellite over a full decade (2008–2017) for monitoring the stratospheric depletion phase  
388 that occurs each year in the S.H. and for investigating its relationship to the NAT formation temperature.  
389 To that end, we focused on and delimited the coldest polar region of the S.H. using a specific PV value  
390 at 530 K (~50 hPa, PV of  $-10 \times 10^{-5} \text{ K.m}^2.\text{kg}^{-1}.\text{s}^{-1}$ ) and stratospheric temperatures at 50 hPa, taken from



391 the ECMWF ERA Interim reanalysis. That single representative pressure level has been considered in  
392 this study given the maximum sensitivity of IASI to HNO<sub>3</sub> around that level, which lies in the range  
393 where the PSCs formation/denitrification processes occur.

394  
395 The annual cycle of total HNO<sub>3</sub>, as observed from IASI, has first been characterized according to the  
396 temperature evolution. Three regimes (R1 to R3) in the total HNO<sub>3</sub> - 50 hPa temperature relationship  
397 were highlighted from the time series over the S.H. polar region: R1 is defined during April and May  
398 and characterized by a rapid decrease in 50 hPa temperatures while HNO<sub>3</sub> accumulates over the pole;  
399 R2, from June to October, follows the onset of the depletion that starts around mid-May in most years  
400 when the 50 hPa temperatures fall below 195 K (considered here as the onset of PSC nucleation phase  
401 at that level), with a strong consistency from year to year; R3, defined from October through March  
402 when total HNO<sub>3</sub> remains at low R2 plateau levels, despite the return of sunlight and heat, characterizes  
403 the strong denitrification of the stratosphere, likely due to PSC sedimentation to lower levels where the  
404 IASI sensitivity is low. For each year over the 10-year study period, the use of the second derivative of  
405 the HNO<sub>3</sub> column versus time was then found to be particularly valuable to detect the onset of the HNO<sub>3</sub>  
406 condensation into PSCs. It is captured, on average from IASI, a few days before June with a delay of 4–  
407 23 days after the maximum in total HNO<sub>3</sub>. The corresponding temperatures ('drop temperatures') were  
408 detected between 189.2 K and 202.8 K ( $194.2 \pm 3.8$  K on average over the 10 years), which tends to  
409 demonstrate the good consistency between the 50 hPa drop temperature and the PSC formation  
410 temperatures in that altitude region. Finally, the annual and spatial variability (within  $1^\circ \times 1^\circ$ ) in the drop  
411 temperature was further explored from IASI total HNO<sub>3</sub>. Inside the isocontours of 195 K for the average  
412 temperatures and of  $-10 \times 10^{-5}$  K.m<sup>2</sup>.kg<sup>-1</sup>.s<sup>-1</sup> for the averaged PV at 530 K, the drop temperatures are  
413 detected between ~mid-May and mid-July, typically range between ~187 K to ~195 K and are associated  
414 with the lowest minima (lower than  $-0.5 \times 10^{14}$  molec.cm<sup>-2</sup>.d<sup>-2</sup>) in the second derivative of the HNO<sub>3</sub> total  
415 column with respect to time, indicating a strong and rapid HNO<sub>3</sub> depletion. Except for unrealistic drop  
416 temperatures (~210 K) that were found in some years above eastern Antarctica and suspected to result  
417 from unfiltered poor quality retrievals arising from emissivity issues above ice, the range of drop  
418 temperatures is interestingly found to be in line with the PSC nucleation temperature that is known, from  
419 previous studies, to strongly depend on several factors (e.g. meteorological conditions, HNO<sub>3</sub> vapour  
420 pressure, temperature threshold exposure, presence of meteoritic dust). At the edge of the vortex,  
421 considering the isocontours of 195 K for the minimum temperatures or of  $-10 \times 10^{-5}$  K.m<sup>2</sup>.kg<sup>-1</sup>.s<sup>-1</sup> for the  
422 minimum PV, higher and later drop temperatures along with weakest minima in the second derivative  
423 of the HNO<sub>3</sub> total column with respect to time, indicating a slow HNO<sub>3</sub> depletion, are found. These  
424 likely result from a short temperature threshold exposure or mixing with already depleted airmasses from  
425 the inner vortex core. The results of this study highlight the ability of IASI to measure the variations in  
426 total HNO<sub>3</sub> and, in particular, to capture and monitor the rapid depletion phase over the whole Antarctic  
427 region.

428  
429 We show in this study that the IASI dataset allows the variability of stratospheric HNO<sub>3</sub> throughout the  
430 year (including the polar night) in the Antarctic to be captured. In that respect, it offers observational  
431 means to monitor the relation of HNO<sub>3</sub> to temperature and the related formation of PSCs. Despite the  
432 limited vertical resolution of IASI which does not allow investigation of the HNO<sub>3</sub> uptake by the  
433 different types of PSCs during their formation and growth along the vertical profile, the HNO<sub>3</sub> total  
434 column measurements from IASI constitute an important new dataset for exploring the strong polar  
435 depletion over the whole stratosphere. This is particularly relevant considering the mission continuity,  
436 which will span several decades with the planned follow-on missions. Indeed, thanks to the three  
437 successive instruments (IASI-A launched in 2006 and still operating, IASI-B in 2012, and IASI-C in  
438 2018) that demonstrate an excellent stability of the Level-1 radiances, the measurements will soon  
439 provide an unprecedented long-term dataset of HNO<sub>3</sub> total columns. Further work could also make use

440 of this unique data set to investigate the relation between HNO<sub>3</sub>, O<sub>3</sub>, and meteorology in the changing  
441 climate.

442  
443

444 **Data availability**

445 The IASI HNO<sub>3</sub> data processed with FORLI-HNO<sub>3</sub> v0151001 are available upon request to the  
446 corresponding author.

447

448 **Author contributions**

449 G.R. and C.W. performed the analysis, wrote the manuscript and prepared the figures. L.C. contributed  
450 to the analysis. S.S., P.-F. C. and L.C. contributed to the interpretation of the results. D.H. was  
451 responsible for the retrieval algorithm development and the processing of the IASI HNO<sub>3</sub> dataset. All  
452 authors contributed to the writing of the text and reviewed the manuscript.

453

454 **Competing interests**

455 The authors declare no competing interests.

456

457 **Acknowledgements**

458 IASI has been developed and built under the responsibility of the Centre National d'Etudes Spatiales  
459 (CNES, France). It is flown on board the Metop satellites as part of the EUMETSAT Polar System. The  
460 IASI L1 data are received through the EUMETCast near-real-time data distribution service. The research  
461 was funded by the F.R.S.-FNRS, the Belgian State Federal Office for Scientific, Technical and Cultural  
462 Affairs (Prodex arrangement 4000111403 IASI.FLOW) and EUMETSAT through the Satellite  
463 Application Facility on Atmospheric Composition Monitoring (ACSAF). G. Ronsmans is grateful to the  
464 Fonds pour la Formation à la Recherche dans l'Industrie et dans l'Agriculture of Belgium for a PhD  
465 grant (Boursier FRIA). L. Clarisse is a research associate supported by the F.R.S.-FNRS. C. Clerbaux is  
466 grateful to CNES for financial support. S. Solomon is supported by the National Science Foundation  
467 (NSF-1539972). We also would like to thank the three reviewers for their helpful comments and  
468 corrections and, in particular, M. Santee for her in-depth reviews, which have substantially improved  
469 the paper quality.

470

471

472

473

474

475

476

477

478

479

480

481

482

483

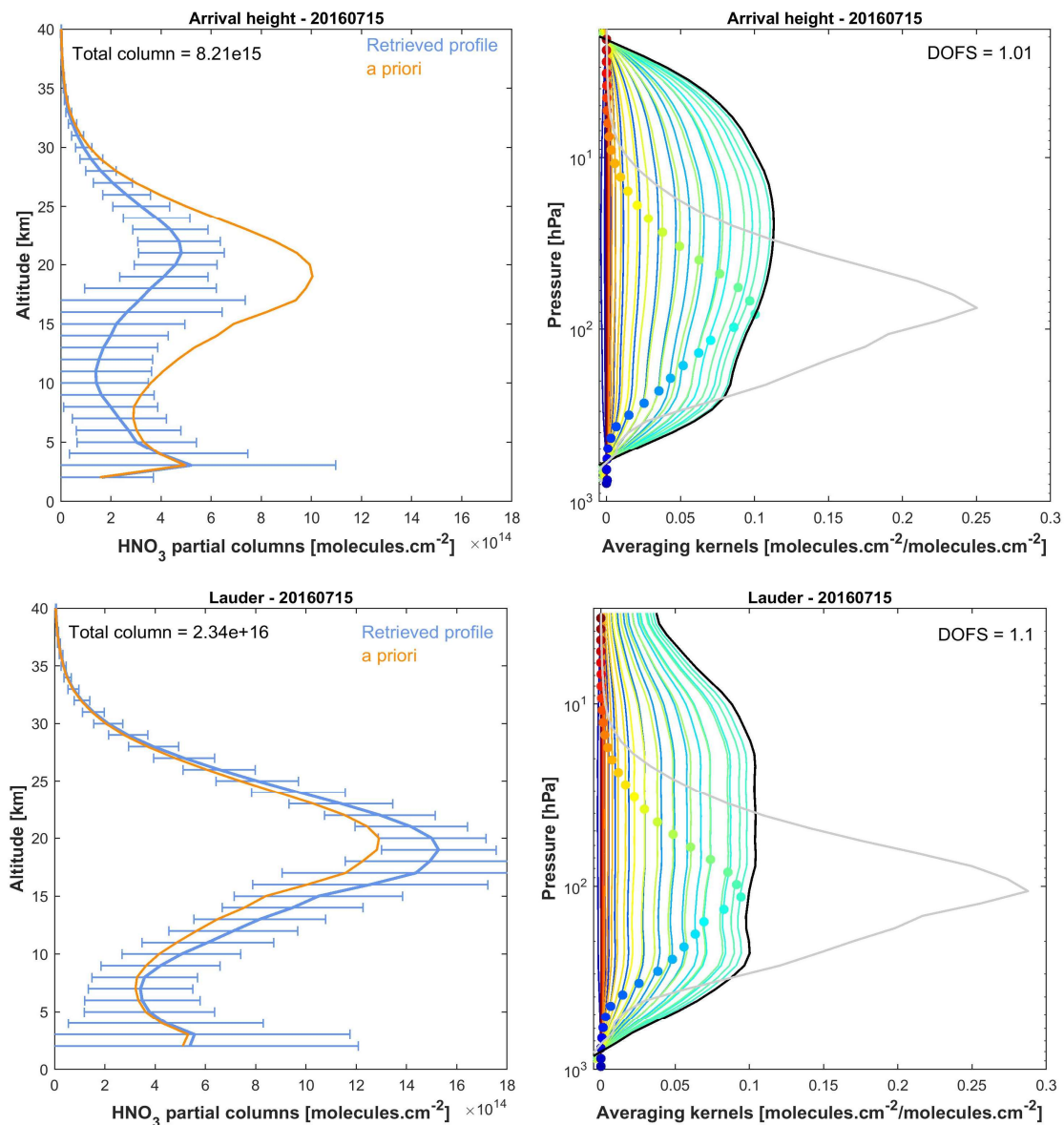
484

485

486

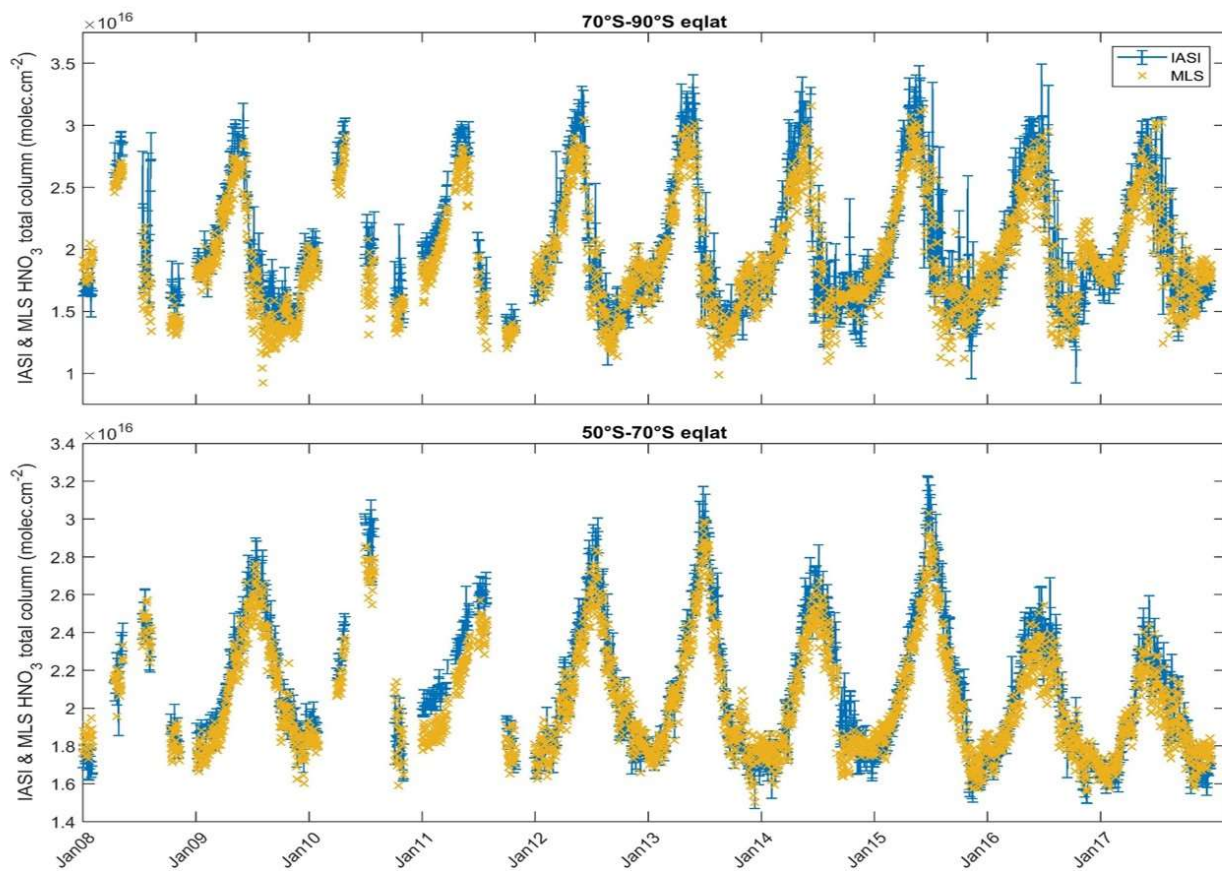
487

488



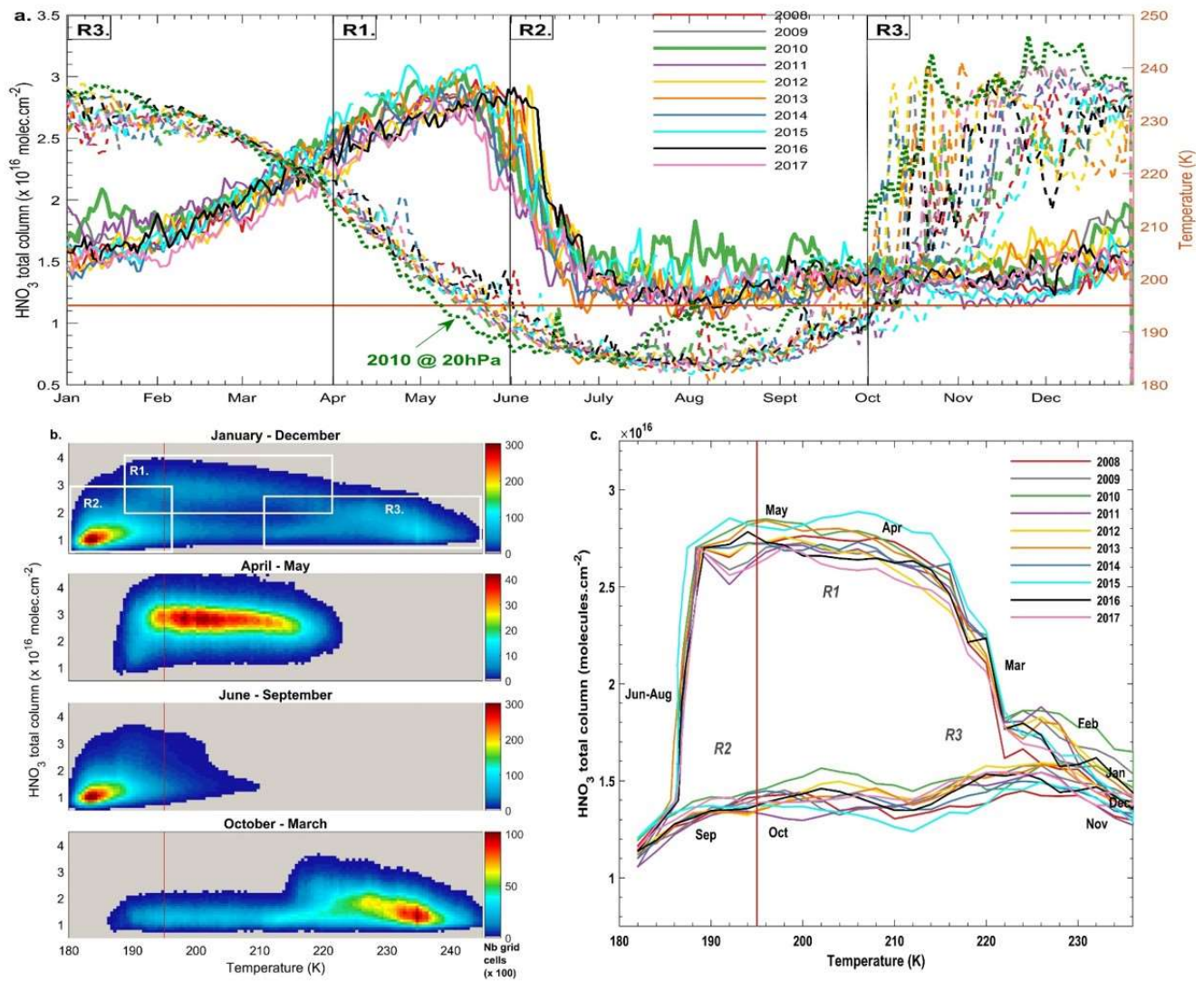
492  
 493  
 494  
 495  
 496  
 497  
 498  
 499  
 500

**Figure 1.** Examples of IASI  $\text{HNO}_3$  vertical profiles (in  $\text{molec.cm}^{-2}$ ) with corresponding averaging kernels (in  $\text{molec.cm}^{-2}/\text{molec.cm}^{-2}$ ; colored lines, with the altitude of each kernel represented by the colored dots) along with the total column averaging kernels (black) and the sensitivity profiles (grey) (both divided by 10) above Arrival Heights (77.49°S, 166.39°E, top panels) and Lauder (45.03°S, 169.40°E; bottom panels). The error bars associated with the  $\text{HNO}_3$  vertical profile represent the total retrieval error. The a priori profile is also represented. The total column and the DOFS values are indicated.



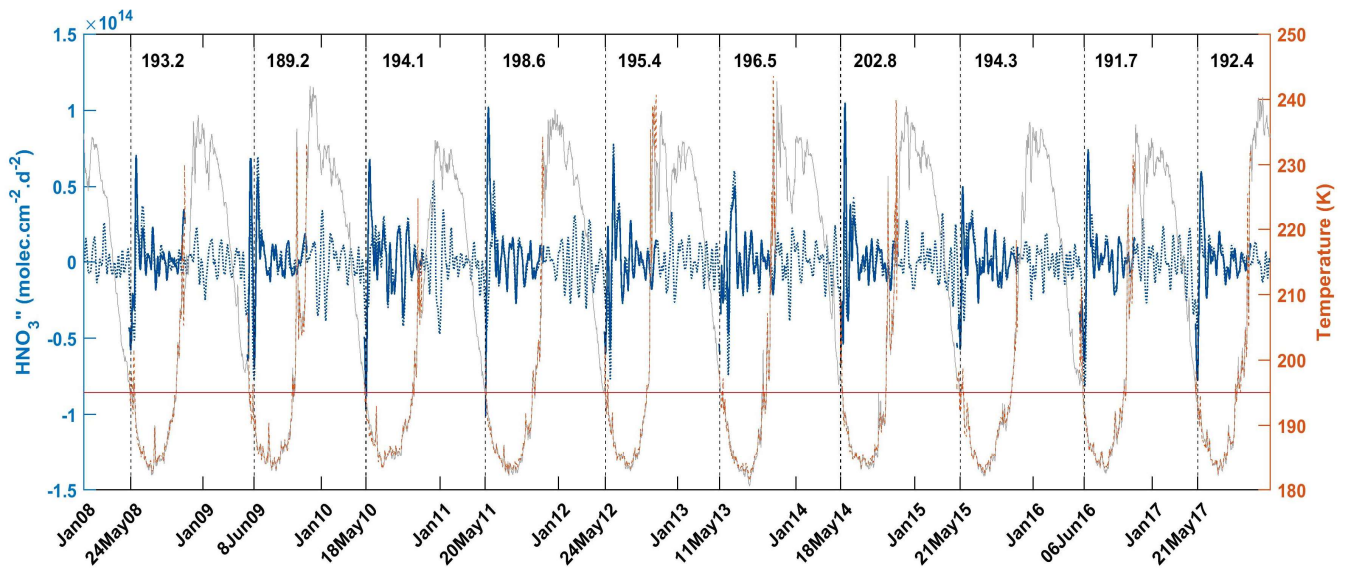
501  
 502  
 503  
 504  
 505  
 506  
 507  
 508  
 509  
 510  
 511  
 512  
 513  
 514  
 515  
 516

**Figure 2.** Time series of daily IASI total HNO<sub>3</sub> column (blue) co-located with MLS and of MLS total HNO<sub>3</sub> columns (orange) within 2.5°x2.5° grid boxes, averaged in the 70°S–90°S (top panel) and the 50°S–70°S (bottom panel) equivalent latitude bands. Note that the MLS total column estimates were obtained by extending the MLS partial stratospheric column values using the FORLI-HNO<sub>3</sub> a priori information (see text for details). The error bars (blue) represent 3σ, where σ is the standard deviation around the IASI HNO<sub>3</sub> daily average.



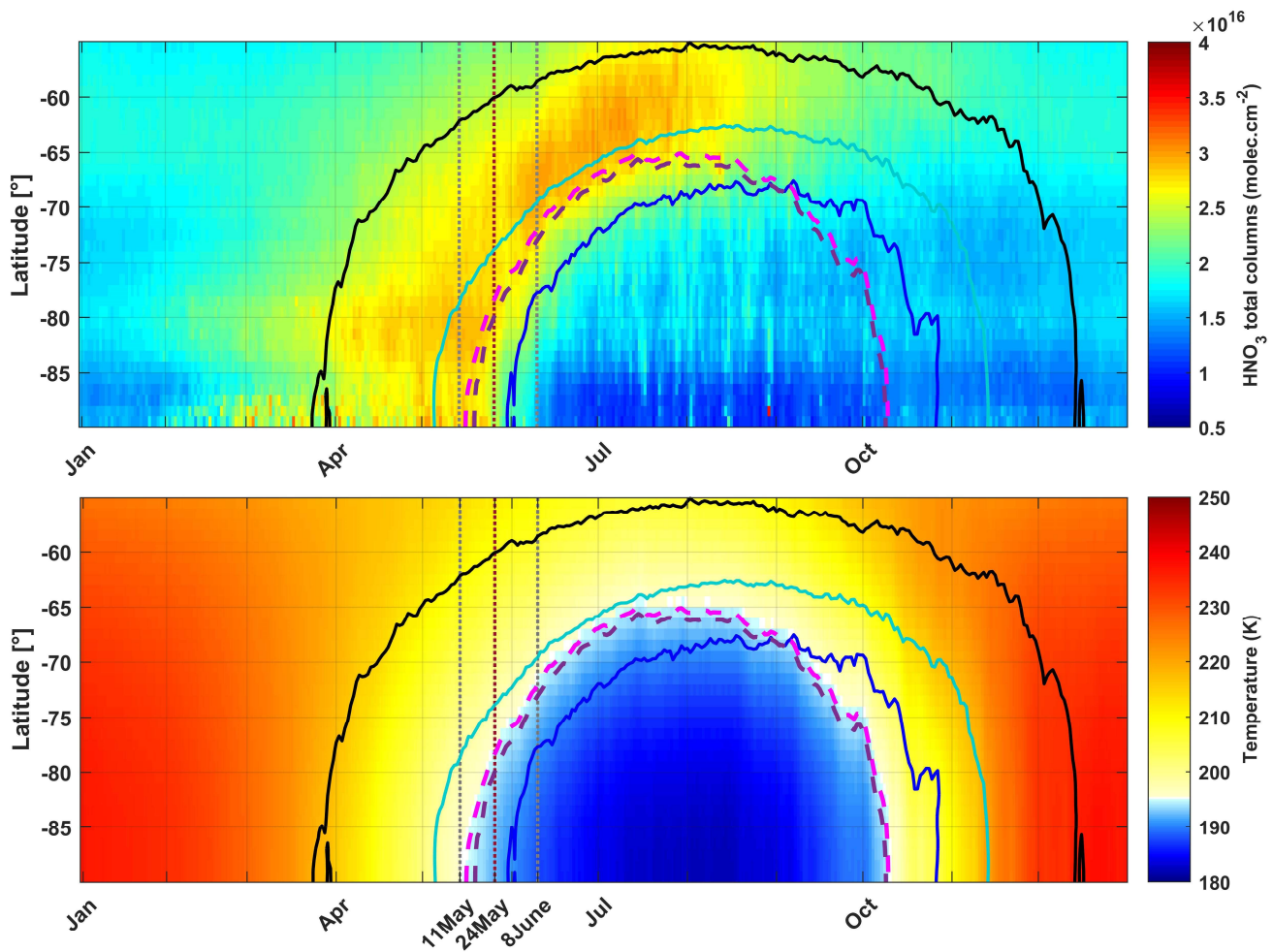
517  
 518  
 519 **Figure 3.** (a) Time series of daily averaged HNO<sub>3</sub> total columns (solid lines) and temperatures taken at 50 hPa  
 520 (dashed lines) in the 70° - 90° S equivalent latitude band, for the years 2008 – 2017. The green dotted line  
 521 represents the temperatures at 20 hPa for the year 2010. (b) HNO<sub>3</sub> total columns versus temperatures (at 50 hPa)  
 522 histogram during the year 2011, over the whole year (top) and for the 3 defined regimes (R1 - R3) separated in  
 523 (a). The colors refer to the number of gridded measurements in each cell. (c) Evolution of daily averaged HNO<sub>3</sub>  
 524 total columns with the highest occurrence (in bins of 0.1×10<sup>16</sup> molec.cm<sup>-2</sup> and 2 K) as a function of the 50 hPa  
 525 temperature for the years 2008 – 2017. The orange horizontal or vertical lines represent the 195 K threshold  
 526 temperature.

517  
 518  
 519  
 520  
 521  
 522  
 523  
 524  
 525  
 526  
 527  
 528  
 529  
 530  
 531  
 532  
 533  
 534



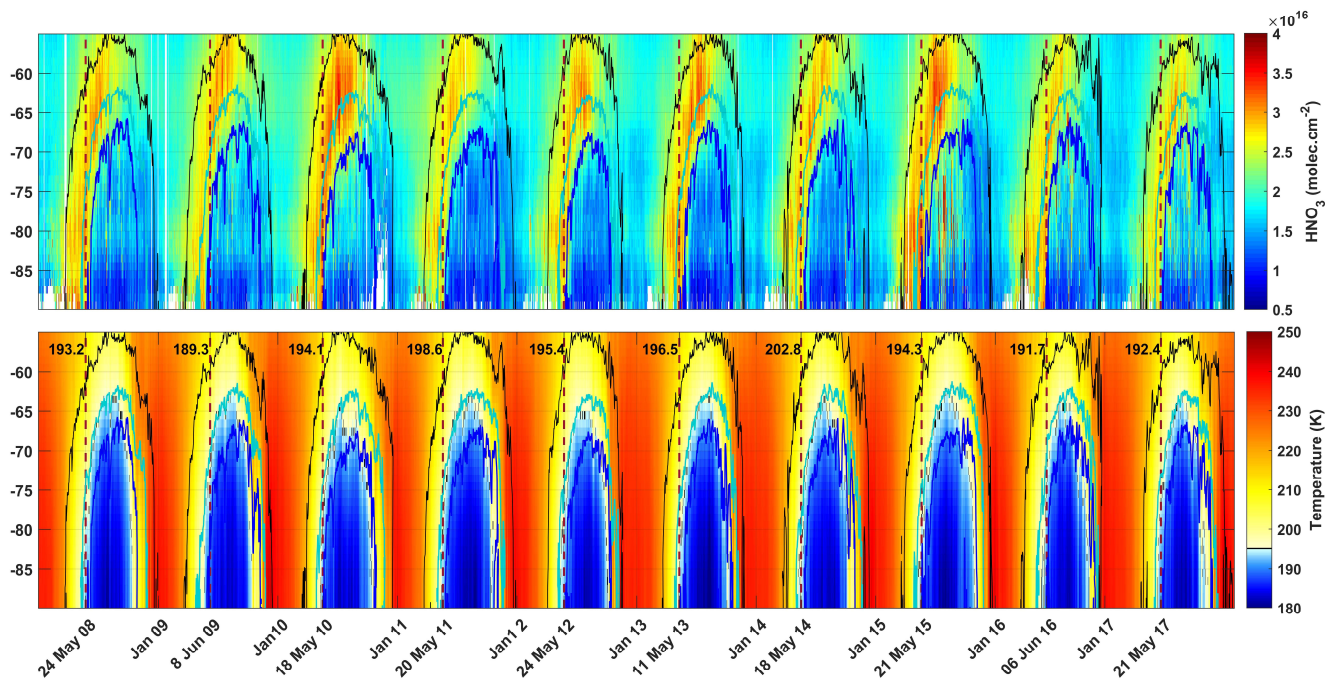
535  
 536  
 537  
 538  
 539  
 540  
 541  
 542  
 543  
 544  
 545  
 546  
 547  
 548

**Figure 4.** Time series of total HNO<sub>3</sub> second derivative (blue, left y-axis) and of the 50 hPa temperature (red, right y-axis), in the region of potential vorticity at 530 K lower than  $-10 \times 10^{-5} \text{ K} \cdot \text{m}^2 \cdot \text{kg}^{-1} \cdot \text{s}^{-1}$ . The red horizontal line corresponds to the 195 K temperature. The vertical dashed lines indicate the second derivative minimum in HNO<sub>3</sub> for each year. The corresponding dates (in bold, on the x-axis) and temperatures are also indicated. The time series of total HNO<sub>3</sub> second derivative (dashed blue) and of temperature (grey) in the 70° – 90° S eqlat band are also represented.



549  
 550  
 551  
 552  
 553  
 554  
 555  
 556  
 557  
 558  
 559

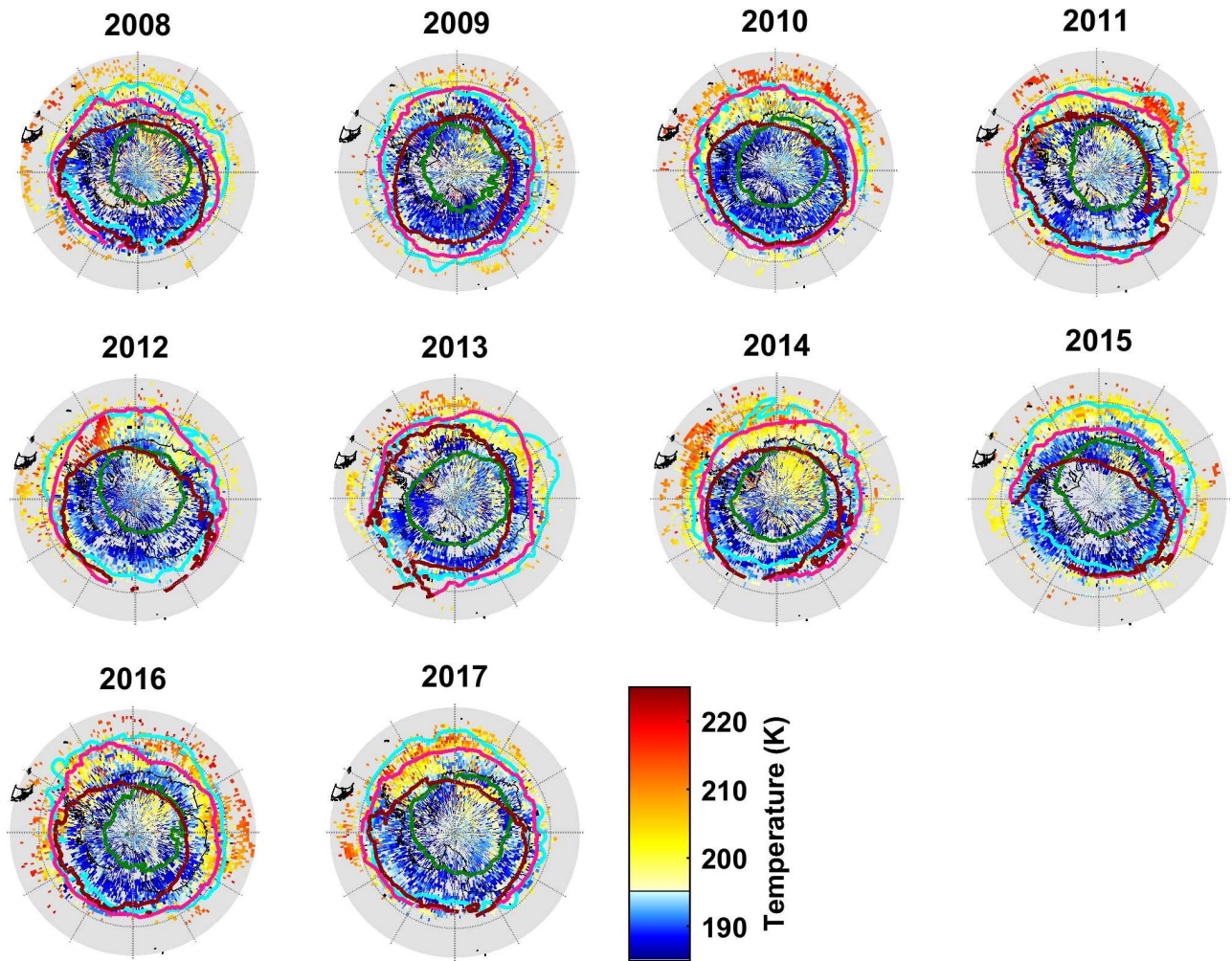
**Figure 5.** Zonal distributions of (a)  $\text{HNO}_3$  total columns (in  $\text{molec.cm}^{-2}$ ) from IASI and (b) temperatures at 50 hPa from ERA Interim (in K) in the  $55^\circ\text{S}$  to  $90^\circ\text{S}$  geographical latitude band and averaged over the years 2008 – 2017. Three isocontours for the climatological (2008-2017) and zonally averaged PV of -5 (black), -8 (cyan) and -10 (blue) ( $\times 10^{-5} \text{K.m}^2.\text{kg}^{-1}.\text{s}^{-1}$ ) at 530 K, as well as the isocontours for the 195 K climatological (2008-2017) zonally averaged temperature (pink) and for the averaged 194.2 K drop temperature (purple) at 50 hPa are superimposed. The vertical grey dashed lines mark the earliest and latest dates for the averaged drop temperature in the 10-year IASI record and the red one indicates the average date for the drop temperatures calculated in the area delimited by the  $-10 \times 10^{-5} \text{K.m}^2.\text{kg}^{-1}.\text{s}^{-1}$  PV contour.



560  
 561  
 562  
 563  
 564  
 565  
 566  
 567  
 568

**Figure 6.** Zonally averaged distributions of (top) HNO<sub>3</sub> total columns (in molec.cm<sup>-2</sup>) from IASI and (bottom) temperatures at 50 hPa from ERA Interim (in K). The geographical latitude range is from 55° to 90° south and the isocontours are PVs of -5 (black), -8 (cyan) and -10 (blue) (× 10<sup>-5</sup> K.m<sup>2</sup>.kg<sup>-1</sup>.s<sup>-1</sup> at 530 K). The vertical red dashed lines correspond to the second derivative minima each year in the area delimited by a -10×10<sup>-5</sup> K.m<sup>2</sup>.kg<sup>-1</sup>.s<sup>-1</sup> PV contour.





569  
 570  
 571  
 572  
 573  
 574  
 575  
 576  
 577  
 578  
 579  
 580  
 581  
 582  
 583  
 584  
 585  
 586  
 587

**Figure 7.** Spatial distribution ( $1^\circ \times 1^\circ$ ) of the drop temperature at 50 hPa (K) (calculated from the total  $\text{HNO}_3$  second derivative minima) for each year of IASI (2008–2017), in a region defined by a PV of  $-8 \times 10^{-5} \text{ K} \cdot \text{m}^2 \cdot \text{kg}^{-1} \cdot \text{s}^{-1}$ . The isocontours of  $-10 \times 10^{-5} \text{ K} \cdot \text{m}^2 \cdot \text{kg}^{-1} \cdot \text{s}^{-1}$  at 530 K for the averaged PV (in green) and the minimum PV (in cyan) encountered over the period 10 May –15 July for each year and the isocontours of 195 K at 50 hPa for the averaged (in red) and the minimum (in pink) temperatures over the same period are represented.

588  
589  
590  
591  
592  
593  
594  
595  
596  
597  
598  
599  
600  
601  
602  
603  
604  
605  
606  
607  
608  
609  
610  
611  
612  
613  
614  
615  
616  
617  
618  
619  
620  
621  
622  
623  
624  
625  
626  
627  
628  
629  
630  
631  
632  
633  
634  
635  
636  
637  
638  
639  
640  
641  
642  
643  
644  
645

## References

- Braun, M., Groöß, J.-U., Woiwode, W., Johansson, S., Höpfner, M., Friedl-Vallon, F., Oelhaf, H., Preusse, P., Ungermann, J., Sinnhuber, B.-M., Ziereis, H., and Braesicke, P.: Nitrification of the lowermost stratosphere during the exceptionally cold Arctic winter 2015/16, *Atmospheric Chemistry and Physics Discussions*, <https://doi.org/10.5194/acp-2019-108>, 2019.
- Carslaw, K. S., Luo, B. P., and Peter, T.: An analytical expression for the composition of aqueous {HNO<sub>3</sub>-H<sub>2</sub>SO<sub>4</sub>-H<sub>2</sub>O} stratospheric aerosols including gas phase removal of HNO<sub>3</sub>, *Geophys. Res. Lett.*, 22, 1877–1880, <https://doi.org/10.1029/95GL01668>, 1995.
- Carslaw, K. S., Wirth, M., Tsias, A., Luo, B. P., Dörnbrack, A., Leutbecher, M., Volkert, H., Renger, W., Bacmeister, J. T., Reimer, E., and Peter, T.: Increased stratospheric ozone depletion due to mountain-induced atmospheric waves, *Nature*, 391, 675–678, <https://doi.org/10.1038/35589>, 1998.
- Clerbaux, C., Boynard, A., Clarisse, L., George, M., Hadji-Lazaro, J., Herbin, H., Hurtmans, D., Pommier, M., Razavi, A., Turquety, S., Wespes, C., and Coheur, P.-F.: Monitoring of atmospheric composition using the thermal infrared IASI/MetOp sounder, *Atmospheric Chemistry and Physics*, 9, 6041–6054, <https://doi.org/10.5194/acp-9-6041-2009>, 2009.
- de Laat, A. T. J. and van Weele, M.: The 2010 Antarctic ozone hole: Observed reduction in ozone destruction by minor sudden stratospheric warmings, *Scientific Reports*, 1, 38, <https://doi.org/10.1038/srep00038>, 2011.
- de Zafra, R. and Smyshlyaev, S. P.: On the formation of HNO<sub>3</sub> in the Antarctic mid to upper stratosphere in winter, *Journal of Geophysical Research*, 106, 23 115, <https://doi.org/10.1029/2000JD000314>, 2001.
- Groöß, J. U., Engel, I., Borrmann, S., Frey, W., Günther, G., Hoyle, C. R., Kivi, R., Luo, B. P., Mollenker, S., Peter, T., Pitts, M. C., Schlager, H., Stiller, G., Vömel, H., Walker, K. a., and Müller, R.: Nitric acid trihydrate nucleation and denitrification in the Arctic stratosphere, *Atmospheric Chemistry and Physics*, 14, 1055–1073, <https://doi.org/10.5194/acp-14-1055-2014>, 2014.
- Hanson, D. and Mauersberger, K.: Laboratory studies of the nitric acid trihydrate: Implications for the south polar stratosphere, *Geophysical Research Letters*, 15, 855–858, <https://doi.org/10.1029/GL015i008p00855>, 1988.
- Harris, N. R. P., Lehmann, R., Rex, M., and von der Gathen, P.: A closer look at Arctic ozone loss and polar stratospheric clouds, *Atmospheric Chemistry and Physics*, 10, 8499–8510, <https://doi.org/10.5194/acp-10-8499-2010>, 2010.
- Hilton, F., Armante, R., August, T., Barnett, C., Bouchard, A., Camy-Peyret, C., Capelle, V., Clarisse, L., Clerbaux, C., Coheur, P.-F., Collard, A., Crevoisier, C., Dufour, G., Edwards, D., Faijan, F., Fourrié, N., Gambacorta, A., Goldberg, M., Guidard, V., Hurtmans, D., Illingworth, S., Jacquinet-Husson, N., Kerzenmacher, T., Klaes, D., Lavanant, L., Masiello, G., Matricardi, M., McNally, A., Newman, S., Pavelin, E., Payan, S., Péquignot, E., Peyridieu, S., Phulpin, T., Remedios, J., Schlüssel, P., Serio, C., Strow, L., Stubenrauch, C., Taylor, J., Tobin, D., Wolf, W., and Zhou, D.: Hyperspectral Earth Observation from IASI: Five Years of Accomplishments, *Bulletin of the American Meteorological Society*, 93, 347–370, <https://doi.org/10.1175/BAMS-D-11-00027.1>, 2012.
- Hoffmann, L., Spang, R., Orr, A., Alexander, M. J., Holt, L. A., and Stein, O.: A decadal satellite record of gravity wave activity in the lower stratosphere to study polar stratospheric cloud formation, *Atmospheric Chemistry and Physics*, 17, 2901–2920, <https://doi.org/10.5194/acp-17-2901-2017>, 2017.
- Höpfner, M., Luo, B. P., Massoli, P., Cairo, F., Spang, R., Snels, M., Di Donfrancesco, G., Stiller, G., von Clarmann, T., Fischer, H., and Biermann, U.: Spectroscopic evidence for NAT, STS, and ice in MIPAS infrared limb emission measurements of polar stratospheric clouds, *Atmospheric Chemistry and Physics*, 6, 1201–1219, <https://doi.org/10.5194/acp-6-1201-2006>, 2006.
- Höpfner, M., Pitts, M. C., and Poole, L. R.: Comparison between CALIPSO and MIPAS observations of polar stratospheric clouds, *Journal of Geophysical Research Atmospheres*, 114, 1–15, <https://doi.org/10.1029/2009JDO12114>, 2009.
- Hoyle, C. R., Engel, I., Luo, B. P., Pitts, M. C., Poole, L. R., Groöß, J. U., and Peter, T.: Heterogeneous formation of polar stratospheric clouds- Part 1: Nucleation of nitric acid trihydrate (NAT), *Atmospheric Chemistry and Physics*, 13, 9577–9595, <https://doi.org/10.5194/acp-13-9577-2013>, 2013.

646  
647 Hurtmans, D., Coheur, P.-F., Wespes, C., Clarisse, L., Scharf, O., Clerbaux, C., Hadji-Lazaro, J., George, M., and Turquety,  
648 S.: FORLI radiative transfer and retrieval code for IASI, *Journal of Quantitative Spectroscopy and Radiative Transfer*, 113,  
649 1391–1408, <https://doi.org/10.1016/j.jqsrt.2012.02.036>, 2012.

650  
651 James, A. D., Brooke, J. S. A., Mangan, T. P., Whale, T. F., Plane, J. M. C., and Murray, B. J.: Nucleation of nitric acid  
652 hydrates in polar stratospheric clouds by meteoric material, *Atmospheric Chemistry and Physics*, 18, 4519–4531,  
653 <https://doi.org/10.5194/acp-18-4519-2018>, 2018.

654  
655 Keys, J. G., Johnston, P. V., Blatherwick, R. D., and Murcray, F. J.: Evidence for heterogeneous reactions in the Antarctic  
656 autumn stratosphere, *Nature*, 361, 49–51, <https://doi.org/10.1038/361049a0>, 1993.

657  
658 Klekociuk, A., Tully, M., Alexander, S., Dargaville, R., Deschamps, L., Fraser, P., Gies, H., Henderson, S., Javorniczky, J.,  
659 Krummel, P., Petelina, S., Shanklin, J., Siddaway, J., and Stone, K.: The Antarctic ozone hole during 2010, *Australian  
660 Meteorological and Oceanographic Journal*, 61, 253–267, <https://doi.org/10.22499/2.6104.006>, 2011.

661  
662 Koop, T., Luo, B., Tsias, A., and Peter, T.: Water activity as the determinant for homogeneous ice nucleation in aqueous  
663 solutions, *Nature*, 406, 611–614, <https://doi.org/10.1038/35020537>, 2000.

664  
665 Lambert, A., Santee, M. L., Wu, D. L., and Chae, J. H.: A-train CALIOP and MLS observations of early winter Antarctic  
666 polar stratospheric clouds and nitric acid in 2008, *Atmospheric Chemistry and Physics*, 12, 2899–2931,  
667 <https://doi.org/10.5194/acp-12-2899-2012>, 2012.

668  
669 Lambert, A., Santee, M. L., and Livesey, N. J.: Interannual variations of early winter Antarctic polar stratospheric cloud  
670 formation and nitric acid observed by CALIOP and MLS, *Atmospheric Chemistry and Physics*, 16, 15 219–15 246,  
671 <https://doi.org/10.5194/acp-16-15219-2016>, 2016.

672  
673 Lambert, A. and Santee, M. L.: Accuracy and precision of polar lower stratospheric temperatures from reanalyses evaluated  
674 from A-Train CALIOP and MLS, COSMIC GPS RO, and the equilibrium thermodynamics of supercooled ternary solutions  
675 and ice clouds, *Atmospheric Chemistry and Physics*, 18, 1945–1975, <https://doi.org/10.5194/acp-18-1945-2018>, 2018.

676  
677 Lowe, D. and MacKenzie, A. R.: Polar stratospheric cloud microphysics and chemistry, *Journal of Atmospheric and Solar-  
678 Terrestrial Physics*, 70, 13–40, <https://doi.org/10.1016/j.jastp.2007.09.011>, 2008.

679  
680 Molleker, S., Borrmann, S., Schlager, H., Luo, B., Frey, W., Klingebiel, M., Weigel, R., Ebert, M., Mitev, V., Matthey, R.,  
681 Woiwode, W., Oelhaf, H., Dörnbrack, A., Stratmann, G., Groß, J.-U., Günther, G., Vogel, B., Müller, R., Krämer, M.,  
682 Meyer, J., and Cairo, F.: Microphysical properties of synoptic-scale polar stratospheric clouds: in situ measurements of  
683 unexpectedly large HNO<sub>3</sub>-containing particles in the Arctic vortex, *Atmospheric Chemistry and Physics*, 14, 10 785–10 801,  
684 <https://doi.org/10.5194/acp-14-10785-2014>, 2014.

685  
686 Murphy, D. M. and Koop, T.: Review of the vapour pressures of ice and supercooled water for atmospheric applications,  
687 *Quarterly Journal of the Royal Meteorological Society*, 131, 1539–1565, <https://doi.org/10.1256/qj.04.94>, 2005.

688  
689 Peter, T.: Microphysics and heterogeneous chemistry of polar stratospheric clouds, *Annual Review of Physical Chemistry*,  
690 48, 785–822, <https://doi.org/10.1146/annurev.physchem.48.1.785>, 1997.

691  
692 Peter, T. and Groß, J.-U.: Chapter 4. Polar Stratospheric Clouds and Sulfate Aerosol Particles: Microphysics, Denitrification  
693 and Heterogeneous Chemistry, in: *Stratospheric Ozone Depletion and Climate Change*, pp. 108–144, Royal Society of  
694 Chemistry, <https://doi.org/10.1039/9781849733182-00108>, 2012.

695  
696 Piccolo, C. and Dudhia, A.: Precision validation of MIPAS-Envisat products, *Atmospheric Chemistry and Physics*, 7, 1915–  
697 1923, <https://doi.org/10.5194/acp-7-1915-2007>, 2007.

698  
699 Pitts, M. C., Poole, L. R., Dörnbrack, A., and Thomason, L. W.: The 2009–2010 Arctic polar stratospheric cloud season: A  
700 CALIPSO perspective, *Atmospheric Chemistry and Physics*, 11, 2161–2177, <https://doi.org/10.5194/acp-11-2161-2011>,  
701 2011.

702

703 Pitts, M. C., Poole, L. R., Lambert, A., and Thomason, L.W.: An assessment of CALIOP polar stratospheric cloud  
704 composition classification, *Atmospheric Chemistry and Physics*, 13, 2975–2988, <https://doi.org/10.5194/acp-13-2975-2013>,  
705 2013.  
706  
707 Pitts, M. C., Poole, L. R., and Gonzalez, R.: Polar stratospheric cloud climatology based on CALIPSO spaceborne lidar  
708 measurements from 2006 to 2017, *Atmospheric Chemistry and Physics*, 18, 10 881–10 913, <https://doi.org/10.5194/acp-18-10881-2018>, 2018.  
709  
710  
711 Rodgers, C. D.: *Inverse Methods for Atmospheric Sounding - Theory and Practice*, vol. 2 of Series on Atmospheric Oceanic  
712 and Planetary Physics, World Scientific Publishing Co. Pte. Ltd., <https://doi.org/10.1142/9789812813718>, 2000.  
713  
714 Roscoe, H. K., Feng, W., Chipperfield, M. P., Trainic, M., and Shuckburgh, E. F.: The existence of the edge region of the  
715 Antarctic stratospheric vortex, *J. Geophys. Res.*, 117, D04301, doi:10.1029/2011JD015940, 2012.  
716  
717 Ronsmans, G., Langerock, B., Wespes, C., Hannigan, J. W., Hase, F., Kerzenmacher, T., Mahieu, E., Schneider, M., Smale,  
718 D., Hurtmans, D., De Mazière, M., Clerbaux, C., and Coheur, P.-F.: First characterization and validation of FORLI-HNO<sub>3</sub>  
719 vertical profiles retrieved from IASI/Metop, *Atmospheric Measurement Techniques*, 9, 4783–4801,  
720 <https://doi.org/10.5194/amt-9-4783-2016>, 2016.  
721  
722 Ronsmans, G., Wespes, C., Hurtmans, D., Clerbaux, C., and Coheur, P.-F.: Spatio-temporal variations of nitric acid total  
723 columns from 9 years of IASI measurements – a driver study, *Atmospheric Chemistry and Physics*, 18, 4403–4423,  
724 <https://doi.org/10.5194/acp-18-4403-2018>, 2018.  
725  
726 Santee, M. L., Manney, G. L., Froidevaux, L., Read, W. G., and Waters, J. W.: Six years of UARS Microwave Limb Sounder  
727 HNO<sub>3</sub> observations : Seasonal, interhemispheric, and interannual variations in the lower stratosphere, *Journal of Geophysical*  
728 *Research*, 104, 8225–8246, <https://doi.org/10.1029/1998JD100089>, 1999.  
729  
730 Santee, M. L., Lambert, A., Read, W. G., Livesey, N. J., Cofield, R. E., Cuddy, D. T., Daffer, W. H., Drouin, B. J., Froidevaux,  
731 L., Fuller, R. A., Jarnot, R. F., Knosp, B. W., Manney, G. L., Perun, V. S., Snyder, W. V., Stek, P. C., Thurstans, R. P.,  
732 Wagner, P. A., Waters, J. W., Muscari, G., de Zafra, R. L., Dibb, J. E., Fahey, D. W., Popp, P. J., Marcy, T. P., Jucks, K. W.,  
733 Toon, G. C., Stachnik, R. A., Bernath, P. F., Boone, C. D., Walker, K. A., Urban, J., and Murtagh, D.: Validation of the Aura  
734 Microwave Limb Sounder HNO<sub>3</sub> measurements, *Journal of Geophysical Research*, 112, 1–22,  
735 <https://doi.org/10.1029/2007JD008721>, 2007.  
736  
737 Schreiner, J., Voigt, C., Weisser, C., Kohlmann, A., Mauersberger, K., Deshler, T., Kröger, C., Rosen, J., Kjöme, N., Larsen,  
738 N., Adriani, A., Cairo, F., Donfrancesco, G. D., Ovarlez, J., Ovarlez, H., and Dörnbrack, A.: Chemical , microphysical , and  
739 optical properties of polar stratospheric clouds, *Journal of Geophysical Research*, 108, 1–10,  
740 <https://doi.org/10.1029/2001JD000825>, 2003.  
741  
742 Sheese, P. E., Walker, K. A., Boone, C. D., Bernath, P. F., Froidevaux, L., Funke, B., Raspollini, P., and von Clarmann, T.:  
743 ACE-FTS ozone, water vapour, nitrous oxide, nitric acid, and carbon monoxide profile comparisons with MIPAS and MLS,  
744 *Journal of Quantitative Spectroscopy and Radiative Transfer*, 186, 63–80, <https://doi.org/10.1016/j.jqsrt.2016.06.026>, 2017.  
745  
746 Snels, M., Scoccione, A., Liberto, L. D., Colao, F., Pitts, M., Poole, L., Deshler, T., Cairo, F., Cagnazzo, C., and Fierli, F.:  
747 Comparison of Antarctic polar stratospheric cloud observations by ground-based and space-borne lidar and relevance for  
748 chemistry–climate models, *Atmospheric Chemistry and Physics*, 19, 955–972, <https://doi.org/10.5194/acp-19-955-2019>,  
749 2019.  
750  
751 Solomon, S.: Stratospheric ozone depletion: A review of concepts and history, *Reviews of Geophysics*, 37, 275–316,  
752 <https://doi.org/10.1029/1999RG900008>, 1999.  
753  
754 Spang, R., Hoffmann, L., Höpfner, M., Griessbach, S., Müller, R., Pitts, M. C., Orr, A. M. W., and Riese, M.: A multi-  
755 wavelength classification method for polar stratospheric cloud types using infrared limb spectra, *Atmospheric Measurement*  
756 *Techniques*, 9, 3619–3639, <https://doi.org/10.5194/amt-9-3619-2016>, 2016.  
757  
758 Spang, R., Hoffmann, L., Müller, R., Groß, J.-U., Tritscher, I., Höpfner, M., Pitts, M., Orr, A., and Riese, M.: A climatology  
759 of polar stratospheric cloud composition between 2002 and 2012 based on MIPAS/Envisat observations, *Atmospheric*  
760 *Chemistry and Physics*, 18, 5089–5113, <https://doi.org/10.5194/acp-18-5089-2018>, 2018.

761  
762 Toon, O. B., Hamill, P., Turco, R. P., and Pinto, J.: Condensation of HNO<sub>3</sub> and HCl in the winter polar stratospheres,  
763 Geophysical Research Letters, 13, 1284–1287, <https://doi.org/10.1029/GL013i012p01284>, 1986.  
764  
765 Tritscher, I., Pitts, M. C., Poole, L. R., Alexander, S. P., Cairo, F., Chipperfield, M. P., et al.: Polar stratospheric clouds:  
766 Satellite observations, processes, and role in ozone depletion, *Reviews of Geophysics*, 59, e2020RG000702,  
767 <https://doi.org/10.1029/2020RG000702>.  
768  
769 Urban, J., Pommier, M., Murtagh, D. P., Santee, M. L., and Orsolini, Y. J.: Nitric acid in the stratosphere based on Odin  
770 observations from 2001 to 2009 – Part 1: A global climatology, *Atmospheric Chemistry and Physics*, 9, 7031–7044,  
771 <https://doi.org/10.5194/acp-9-7031-2009>, 2009.  
772  
773 Voigt, C., Schreiner, J., Kohlmann, A., Zink, P., Mauersberger, K., Larsen, N., Deshler, T., Kro, C., Rosen, J., Adriani, A.,  
774 Cairo, F., Donfrancesco, G. D., Viterbini, M., Ovarlez, J., Ovarlez, H., and David, C.: Nitric Acid Trihydrate (NAT) in Polar  
775 Stratospheric Clouds, *Science*, 290, 1756–1758, <https://doi.org/10.1126/science.290.5497.1756>, 2000.  
776  
777 Voigt, C., Larsen, N., Deshler, T., et al.: In situ mountainwave polar stratospheric cloud measurements: Implications for nitric  
778 acid trihydrate formation, *J. Geophys. Res.*, 108(D5), doi:10.1029/2001JD001185, 2003.  
779  
780 Voigt, C., Schlager, H., Luo, B. P., Dörnbrack, A., Roiger, A., Stock, P., Curtius, J., Vössing, H., Borrmann, S., Davies, S.,  
781 Konopka, P., Schiller, C., Shur, G., and Peter, T.: Nitric Acid Trihydrate (NAT) formation at low NAT supersaturation in  
782 Polar Stratospheric Clouds (PSCs), *Atmospheric Chemistry and Physics*, 5, 1371–1380, [https://doi.org/10.5194/acp-5-1371-](https://doi.org/10.5194/acp-5-1371-2005)  
783 2005, 2005.  
784  
785 von König, M.: Using gas-phase nitric acid as an indicator of PSC composition, *Journal of Geophysical Research*, 107,  
786 <https://doi.org/10.1029/2001jd001041>, 2002.  
787  
788 Wang, X. and Michelangeli, D. V.: A review of polar stratospheric cloud formation, *China Particuology*, 4, 261–271,  
789 [https://doi.org/10.1016/S1672-2515\(07\)60275-9](https://doi.org/10.1016/S1672-2515(07)60275-9), 2006.  
790  
791 Wegner, T., Groß, J.-U., von Hobe, M., Stroh, F., Sumin'ska-Ebersoldt, O., Volk, C. M., Hösen, E., Mitev, V., Shur, G.,  
792 and Müller, R.: Heterogeneous chlorine activation on stratospheric aerosols and clouds in the Arctic polar vortex,  
793 *Atmospheric Chemistry and Physics*, 12, 11 095–11 106, <https://doi.org/10.5194/acp-12-11095-2012>, 2012.  
794  
795 Wespes, C., Hurtmans, D., Clerbaux, C., and Coheur, P.-F.: O<sub>3</sub> variability in the troposphere as observed by IASI over 2008–  
796 2016: Contribution of atmospheric chemistry and dynamics, *Journal of Geophysical Research: Atmospheres*, 122, 2429–  
797 2451, <https://doi.org/10.1002/2016JD025875>, <http://doi.wiley.com/10.1002/2016JD025875>, 2017.  
798  
799 WMO: Scientific Assessment of Ozone Depletion: 2014, Global Ozone Research and Monitoring Project – Report No. 55,  
800 World Meteorological Organization, Geneva, Switzerland, 2014.  
801  
802 Zhu, Y., Toon, O. B., Lambert, A., Kinnison, D. E., Brakebusch, M., Bardeen, C. G., Mills, M. J., and English, J. M.:  
803 Development of a Polar Stratospheric Cloud Model within the Community Earth System Model using constraints on Type I  
804 PSCs from the 2010-2011 Arctic winter, *Journal of Advances in Modeling Earth Systems*, 7, 551–585,  
805 <https://doi.org/10.1002/2015ms000427>, 2015.  
806  
807 Zondlo, M. A., P. K. Hudson, A. J. Prenni, and M. A. Tolbert: Chemistry and microphysics of polar stratospheric clouds and  
808 cirrus clouds, *Annu. Rev. Phys. Chem.*, 51, 473–499, 2000.